MATERIALS SCIENCE

Ionic communication for implantable bioelectronics

Zifang Zhao[1], George D. Spyropoulos[1]†, Claudia Cea[1], Jennifer N. Gelinas[2,3]*, Dion Khodagholy[1]*

Implanted bioelectronic devices require data transmission through tissue, but ionic conductivity and inhomogeneity of this medium complicate conventional communication approaches. Here, we introduce ionic communication (IC) that uses ions to effectively propagate megahertz-range signals. We demonstrate that IC operates by generating and sensing electrical potential energy within polarizable media. IC was tuned to transmit across a range of biologically relevant tissue depths. The radius of propagation was controlled to enable multiline parallel communication, and it did not interfere with concurrent use of other bioelectronics. We created a fully implantable IC-based neural interface device that acquired and noninvasively transmitted neurophysiologic data from freely moving rodents over a period of weeks with stability sufficient for isolation of action potentials from individual neurons. IC is a biologically based data communication that establishes long-term, high-fidelity interactions across intact tissue.

INTRODUCTION

Implanted bioelectronic devices are increasingly being used to monitor and treat disease (*1*–*3*). Signal transmission from the implanted device to the external electronics is a major challenge for safe, effective, and long-term use. Physiologic signals are robustly transmitted by cables because of their simplicity and high data rate capacity, but this approach requires permanent tissue-traversing components that limit their use in chronic applications. Wireless data transmission from implanted devices has been accomplished using radio frequency (RF) and ultrasound-based communication (*4*–*10*). The complex, high-power consumption, nonbiocompatible, and rigid RF electronic components combined with the high ionic conductivity of biological tissue place severe restrictions on its signal transmission capabilities (*11*–*13*). As a result, the majority of RF-based systems require tissue-extruding components that interface with a transmitter placed outside the body (*14*, *15*). Although ultrasound has better tissue penetration than RF, communication is strongly dependent on the coupling factor between the transmitter and receiver, allowing tissue inhomogeneity and mechanical movements to introduce instability (*5*, *7*, *8*, *10*, *16*). Optical methods have high power consumption and are limited by light scattering within tissue (*17*). Therefore, approaches that harmonize with the properties of biological tissue to facilitate simple, yet reliable, data transmission are lacking. Intrabody communication that uses ion-conducting tissue as the medium to transmit information has been proposed. Signals have been transmitted across the tissue surface using externally applied electric potential, and this circuit is completed by capacitive coupling (CC) with the surrounding environment (air) (*18*, *19*). Therefore, this approach cannot be used for transmission from a fully implanted device because a permanent conduit with the environment is required to complete the circuit. Because the signal is transmitted by ion transport between transmitter and receiver, speed of communication is also dictated by ion mobility (*20*).

Neuroelectronic devices have some of the most demanding requirements for data transmission because of the high spatial and temporal sampling required to interpret and modulate brain activity (*21*). Sampling neural activity at several kilohertz per second from multiple electrodes improves representation of activity patterns and allows targeted feedback (*22*–*24*). These devices are currently used to diagnose and treat neuropsychiatric disorders (*25*–*27*), decode neural representations for brain-machine interfaces (*28*, *29*), and establish the functional relevance of neural activity (*30*). However, data transmission challenges complicate clinical device implementation. For instance, brain-machine interfaces to enable control of assistive movement and communication devices in paralyzed patients require a chronically implanted, bulky, and rigid transcutaneous port that transmits high spatiotemporal resolution neural signals from a microelectrode array to external processors (*28*). Bioelectronics for responsive neurostimulation to abort seizures (NeuroPace) are fully implanted and communicate using RF, but necessitate a large, rigidly encapsulated processing unit, and the number of transmitted channels is limited (*31*).

Here, we introduce ionic communication (IC) that leverages ions in biologic tissue to propagate megahertz-range signals. We demonstrate that IC operates by generating and sensing stored electrical potential energy within polarizable media in a frequency-dependent manner. We determined the geometric properties that govern IC transmission depth and controlled transmission radius to permit multiline parallel communication. We integrated IC with advanced neural interfaces to create a fully implantable device capable of acquisition and noninvasive transmission of neurophysiologic data from freely moving rats over a period of weeks. IC enabled a stable, efficient link with implanted components and had communication efficiency (data rate/power consumption) several orders of magnitude above other approaches used with implantable bioelectronics. We used IC for real-time transmission of multichannel local field potential (LFP) and neural spiking data, with data quality sufficient for clustering of individual neuronal action potentials. IC creates a high-speed, low-power link between implanted and external electronics with the potential to enhance the safety and efficiency of a wide range of bioelectronic devices.

[1]Department of Electrical Engineering, Columbia University, New York, NY 10027, USA. [2]Department of Neurology, Columbia University Medical Center, New York, NY 10032, USA. [3]Institute for Genomic Medicine, Columbia University Medical Center, New York, NY 10032, USA.
*Corresponding author. Email: jng2146@cumc.columbia.edu (J.N.G.); dk2955@columbia.edu (D.K.)
†Present address: Department of Information Technology Waves, Ghent University, Technology Campus, Technologiepark 126, Zwijnaarde, Gent 9052 Belgium.

RESULTS

Polarizability governs a material's dielectric constant (also known as relative permittivity) and reflects the frequency-dependent ability to store potential energy under the influence of an electric field. Electromagnetic waves are efficiently generated and propagated within low relative permittivity materials. As the relative permittivity increases, more energy is stored in the material, and the transmission efficiency decreases (*11*–*13*). When materials contain charge carriers, such as electrons or ions, electromagnetic energy is also converted into conduction currents, impeding generation and limiting propagation to the material's specific skin depth in a frequency-dependent manner (*32*). Therefore, the ion-rich, aqueous nature of biological tissue limits use of RF technologies in implantable devices. We hypothesized that we could transmit electrical signals by sensing the stored electrical potential energy within the tissue rather than relying on an implanted antenna. Application of alternating potential across a pair of implanted electrodes would transfer energy into the tissue, with efficiency dictated by the material's conductivity and polarizability, as well as the frequency of the applied potential.

To test this hypothesis, we first developed an experimental setup consisting of two pairs of Au-based electrodes with identical geometry placed parallel to each other across a medium to simulate tissue (Fig. 1A). In this manner, one pair serves as a signal transmitter (TX, implanted) that is connected to a constant amplitude frequency sweep signal from 1 Hz to 10 MHz, and the second pair functions as a receiver (RX, on the surface), permitting differential amplification of the transmitted potential across its constituent electrodes. To evaluate the capacity of such a device to establish a communication link across tissue, we performed frequency response measurements from the RX in media with varying ion concentrations of phosphate-buffered saline (PBS; 10^{-3}, 10^{-2}, 10^{-1}, and 1×; Fig. 1B and figs. S1 and S2). Each frequency response curve was characterized by an inverted U pattern, with increasing response between 1 Hz and 1 KHz, an intervening plateau, and decreasing response above 10 KHz to 100 MHz. Increasing ion concentration shifted the curve to the right, resulting in maximal response at higher frequencies relative to lower ion concentrations. We attributed these responses to a combination of properties derived from the (i) electrode/electrolyte interface and (ii) material composition of the electrolyte. We investigated this electrode/electrolyte interface, which is modeled by a resistive-capacitive (RC) circuit due to the existence of electric double layer capacitance (EDL) (*33*), by performing electrochemical impedance spectroscopy (EIS) using the same electrodes and media. At low frequencies (<1 KHz), the interface is dominated by the capacitive component of the EDL, and we found that the impedance (Z) was independent of the medium's ion concentration (Fig. 1C, yellow shading, and fig. S3). At higher frequencies, the contribution of this capacitance to the impedance becomes negligible ($Z \sim 1/C$), and the impedance is governed by the resistive component. In keeping with this notion, higher ion concentrations resulted in lower impedance at these frequencies (Fig. 1C, red shading). The material composition of the electrolyte can also be modeled as an RC, with the resistive component arising from the strength of ionic conduction, and the capacitive component is determined by the polarizability (quantified by relative permittivity, ε_r) (*34*). These results suggest that the frequency response curves of IC can be separated into two regimes: (i) EDL-RC dominated (yellow) at low frequencies and (ii) medium-RC dominated at higher frequencies (red), generating a medium-specific bandpass of maximal IC response (Fig. 1D). Consistent with this model, media with very low ion concentration [deionized water (DI)] exhibited less response than ionic electrolytes and a further left-shifted frequency response curve (Fig. 1B, gray). Media with low polarizability [isopropyl alcohol (IPA)] had the lowest response across the spectrum (Fig. 1B, red). Ionic aqueous solutions, such as those that comprise the extracellular space of tissue, are therefore optimally situated to maximally transmit alternating potential at high frequencies.

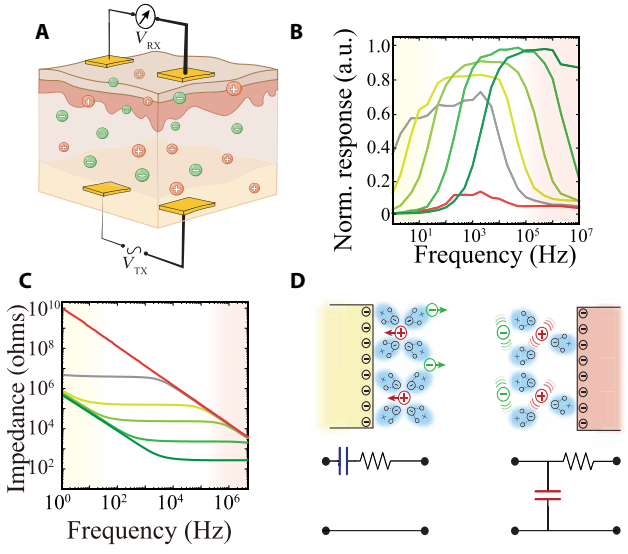

Fig. 1. Configuration and characterization of IC. (**A**) Cross-sectional schematic illustration of an IC device consisting of an implanted transmitter (TX) electrode pair inside a biological tissue with ionic charge carriers [anions (green) and cations (red)], and a receiver electrode pair (RX) on the surface of the tissue. V_{TX} denotes the transmitter signal, while V_{RX} represents the measured voltage from the RX outside of tissue. (**B**) Frequency responses of IC acquired in 10^{-3}, 10^{-2}, 10^{-1}, and 1× PBS (darker shades represent higher concentrations), deionized water (DI; gray), and isopropyl alcohol (IPA; red) with a 1-Hz to 10-MHz V_{TX} sweep signal. Interelectrode spacing and distance between TX and RX arrays were fixed at 25 mm. a.u., arbitrary units. (**C**) Electrochemical impedance of an IC electrode as a working electrode in the same media as (B); color scheme as per (B). Ag/AgCl electrodes were used as counter and reference electrodes. (**D**) Schematic of EDL capacitance (yellow, top left) at electrode/electrolyte interface and its corresponding simplified series RC model (bottom left). Schematic of capacitance resulting from media polarizability (red, top right) and its parallel RC model (bottom right).

Next, we established that IC is distinct from intrabody communication approaches both with regard to its operating mechanism and performance. We designed experiments that directly compared the performance of IC with CC and galvanic coupling (GC)–based communication for implantable devices. Intrabody CC uses cutaneous tissue and the environment (air) between RX and TX terminals as communication medium (Fig. 2A, top). As its name implies, this circuit is composed of a capacitor formed by the air/environment as dielectric between RX and TX terminals (Fig. 2A, top highlighted in yellow) (*18*, *35*). Therefore, the simplified circuit diagram of CC is composed of two paths between TX (source) and RX (measure): (i) a lateral cutaneous path consisting of the tissue impedance (Z_T) in series with the electrode/tissue interface impedance, defined by the tissue's electrochemical properties, electrode materials, and effective electrode area, and (ii) an environmental path consisting of the environmental capacitance (C_{env}), defined by the size of the RX and

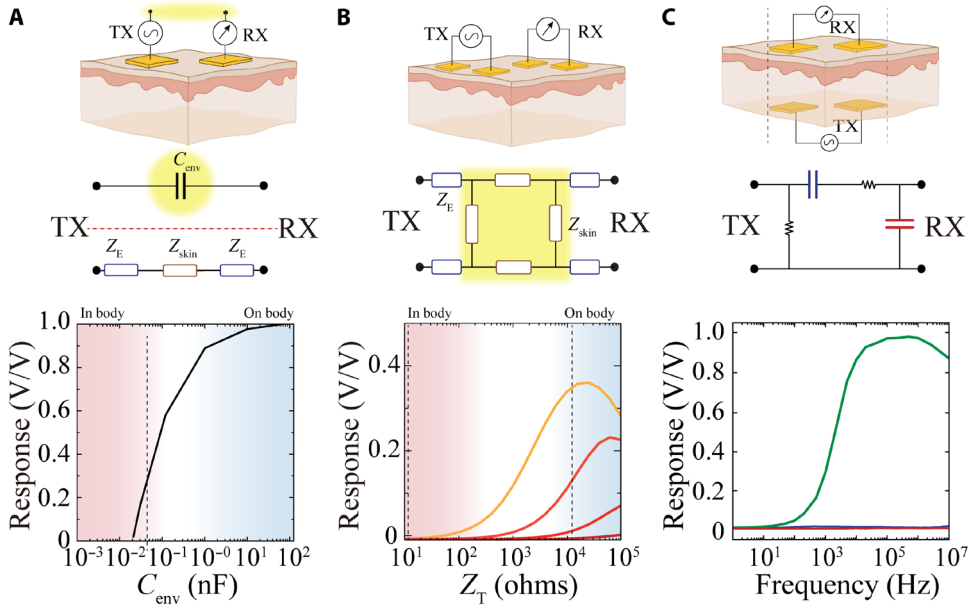

Fig. 2. Comparison of IC with capacitive (CC) and galvanic (GC) intrabody communication. (**A**) Cross-sectional schematic illustrating location and arrangement of TX and RX for CC. Highlighted area illustrates the environmental capacitance (C_{env}) between RX and TX via shared environment (top). Corresponding simplified circuit model of CC; Z_E = electrode/body interface impedance, Z_{skin} = tissue impedance. Yellow highlighted area emphasizes the necessity of a capacitive return path through the environment (middle). Normalized response defined by the ratio of V_{TX} and V_{RX} as a function of C_{env}. Blue area localizes the range of achievable capacitance values when the electrodes are on a tissue surface or outside body. Red area marks the effective capacitance when electrodes are placed within tissue. (**B**) Cross-sectional schematic illustrating location and arrangement of TX and RX for GC. Corresponding simplified circuit model of GC with similar notation as (A). The highlighted area emphasizes the necessity of high overall tissue impedance to create a voltage divider (middle). Normalized response, as in (A), as a function of tissue impedance (Z_T). The superimposed curves show TX with 10^3 to 10^6 ohms (orange to red, respectively) impedances (Z_E). Blue area localizes the range impedances for the tissue surface. Red area marks impedance ranges within tissue. (**C**) Cross-sectional schematic illustrating location of TX and RX for IC. TX is implanted within tissue, and RX is placed on the external tissue surface. The dashed lines indicate that TX and RX are aligned (top). Corresponding simplified circuit model of IC that accounts for EDL capacitance in blue and capacitance from polarizability of water in red (middle). Frequency responses of IC (black), as well as implanted configurations of CC (red) and GC (blue). Au-based TX and RX electrodes (25 mm) were used in PBS for all experiments.

TX electrodes and the dielectric properties of the environment and air (Fig. 2A, middle). The value of C_{env} plays a critical role in the feasibility and stability of communication between RX and TX. Higher values of C_{env} result in lower impedance of the environmental path and robust communication via CC. Even when C_{env} is high (Fig. 2A, blue zone), only short-term exchange of small data packets, such as business card information, is possible because changes in the environment (e.g., air flow and lighting) directly affect C_{env} and, hence, the stability of the link. To create an implantable device based on CC, the environmental path must be within the body. However, the high ion concentration of body tissue reduces the capacitance of the environmental path to several orders of magnitude lower than that required for CC-based communication (Fig. 2A, bottom). To increase the stability of the environmental path, intrabody GC was introduced (*36*). GC replaced the environmental path of CC with another cutaneous path by placing both pairs of RX and TX on the tissue surface (Fig. 2B, top). The simplified circuit model of GC is composed of four electrode/tissue interface impedances connected to a network of tissue impedances. When the electrode/tissue interface impedance is low relative to the tissue impedance, a practical voltage division that allows communication is established. Low interface impedance is typically accomplished by using large electrodes. In this manner, the circuit impedances can also remain constant and independent of the environment, providing more communication stability compared to CC. An implantable device based on GC requires the TX to be moved from a position on the tissue surface, where tissue impedance is high (Fig. 2B, bottom, blue zone), to within the tissue, where impedance is much lower (Fig. 2B, bottom, red zone) (*37*, *38*). Tissue impedance in this arrangement only sufficiently exceeds interface impedance at low frequencies (~KHz regime) and when interface impedance is maximally decreased (e.g., by increasing electrode size; Fig. 2B, lighter-shaded curves), precluding practical use.

In contrast to CC and GC, IC is specifically designed for use with fully implantable devices, where TX is within tissue and RX is on the surface (Fig. 2C, top). On the basis of electrochemical impedance and frequency measurements performed in the presence of varying ion concentrations and media polarizability (Fig. 1), we defined the IC-simplified circuit model as a bandpass filter. The EDL between the tissue and electrode (Fig. 2C, middle, series blue capacitor) accounts for the high-pass regime (rising section of curves in Fig. 1B), whereas the capacitance due water polarization in the presence of physiologic concentrations of ions (Fig. 2C, middle, parallel red capacitor) defines the low-pass regime (falling section of curves in Fig. 1B). The high ion concentration and water content of tissue results in an effective bandpass (flat area of the curves in Fig. 1B) between 10^5 and 10^7 Hz, optimal for high-speed communication (Fig. 2C, bottom, green trace). We directly and experimentally compared the performance of CC, GC, and IC in a fully implanted configuration. All electrodes and geometries were kept constant across

the communication methods. We found that IC (Fig. 2C, bottom, green trace) maintained a high constant response at megahertz frequencies, whereas CC (red) and GC (blue) exhibited negligible responses across the frequency spectrum, with no effective signal received (Fig. 2C, bottom). Therefore, CC and GC cannot serve as data transmission methods for fully implantable devices, and IC is a practically and mechanistically distinct, effective method for this purpose.

After establishing IC as a potentially viable strategy for implantable device communication, we began investigating electrode/electrolyte interface by examining the effect of TX/RX electrode material composition and geometry on the IC frequency response. We fabricated Au and conducting polymer-based [poly(3,4-ethylenedioxythiophene)–polystyrenesulfonate (PEDOT:PSS)] IC electrode pairs spanning two orders of magnitude in size. It is known that conducting polymers reduce the electrochemical impedance of noble metals (*39*). This impedance reduction is primarily mediated by increased uptake of ions across the bulk of the hydrophilic PEDOT:PSS film, which enlarges the electrode/electrolyte capacitance (*40*, *41*). We found that the conducting polymer resulted in higher capacitance (lower impedance) than Au for a given electrode size at low frequencies and that the impedances became equivalent at high frequencies. However, the corner frequency (f_c) of the EIS curves was left-shifted for a PEDOT:PSS compared to an Au electrode of the same size. Larger electrode size was associated with decreased impedance across the frequency spectrum (Fig. 3A and fig. S4). We observed that the EIS f_c was equivalent to the corner frequency of the IC frequency response curve (f_{IC}; Fig. 3B and fig. S5), suggesting that the EDL plays a critical role in the effective bandwidth for IC operation. Extracting f_{IC} for the electrodes characterized in Fig. 3A revealed that use of conducting polymer as TX/RX electrode material extends the bandwidth for IC by two orders of magnitude for any given electrode size (Fig. 3C). Therefore, although improving the electrochemical capacitance of the TX/RX does not directly affect the signal response for IC, it enables a wider range of IC operating frequencies with smaller electrodes.

We next asked across what tissue distance IC could effectively transmit. We fabricated IC RX/TX pairs with geometries spanning two orders of magnitude in their length (L), distance between electrodes in a pair (W), and the distance between the TX and RX pairs (D), and measured the frequency response curves for each configuration. IC response was linearly and independently correlated with each measure, increasing proportionally with L and W, but decreasing with D (Fig. 4, A and B, and figs. S6 and S7). Hence, any combination of L and W that resulted in the same multiplicative product was associated with the same D. Effective signal acquisition at the RX is also affected by the voltage of signal applied to the TX. To understand the relationship between these factors, we determined the maximal D across which signals could be reliably acquired at each combined geometry ($L \times W$) for four different TX signal voltages (Fig. 4C and fig. S7). At an operating voltage of 50 mV, a combined geometry of 9 mm^2 [which could be achieved, for example, by a configuration of a 3-mm RX/TX electrode length (L) with 3 mm between the electrodes of the TX (W)] resulted in a transmission depth of 50 mm. At the lowest operating voltage tested (1 mV), a transmission depth of 50 mm necessitated increasing the combined geometry to 200 mm^2 (which could be achieved, for example, by a configuration of L = 10 mm and W = 20 mm). Therefore, a range of IC electrode geometries compatible with implantation were capable of communicating across distances required to target a variety of tissue, from human skin to visceral organs. We furthermore directly compared the transmission depth of IC (L = 1 mm) with a Bluetooth Low Energy (BLE) protocol and found that the RF-based system had markedly higher signal attenuation in physiological environments. RF, in contrast to IC, was unable to establish a transmission link at distances further than 50 mm, and the RF signal attenuation at the smallest measurable depth was greater than IC signal attenuation at a depth of 100 mm (fig. S8).

Digital communication is often an optimal approach because it preserves signal quality, allowing for error correction, encryption, and narrow bandwidth transmission. Because IC effectively transmits high-frequency signals, it is primed for use with digital communication protocols. To explore this application, we used a set of TX/RX electrodes across electrolyte to transmit digital pulses. To convert the received signals into a digital stream and simultaneously eliminate amplitude variations due to changes in electrode/electrolyte potential, we used an automatic variable gain differential amplifier at the RX (fig. S9 and Materials and Methods). This design maintained a constant signal root mean square (RMS) over a defined window (10 μs), which was substantially longer than individual pulses transmitted (0.1 to 1 μs; fig. S10). We found that the rise/fall time of the pulse (τ) after differential amplification was 7.1 ns

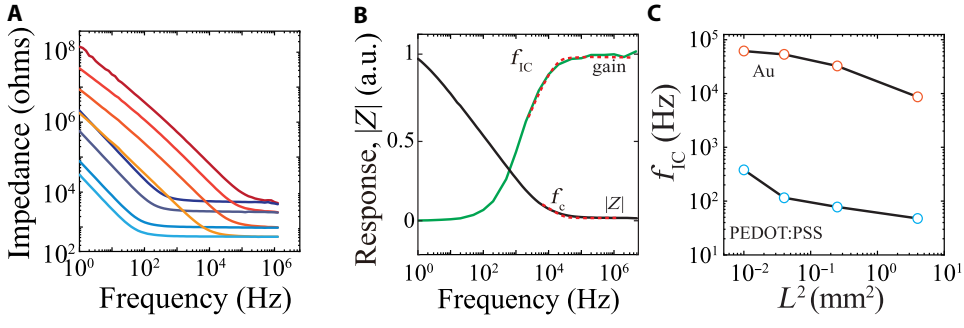

Fig. 3. Use of conducting polymers lowers electrochemical impedance to expand the range of effective IC operation frequencies. (**A**) Electrochemical impedance of conducting polymer–based (shades of blue) and Au-based (shades of red) IC electrodes with 0.5-, 1-, 2-, and 5-mm length (darker shades represent shorter lengths). (**B**) Normalized IC response (green) and electrochemical impedance (black) spectrum of an IC electrode (W, L, D = 5 mm) highlighting the alignment of Fc and F_{IC}. The red dashed superimposed lines are exponential fits of the response and impedance curves that resulted into f_c = 8.63 KHz and f_{IC} = 8.71 KHz. (**C**) Turning frequency of Au and PEDOT:PSS–based electrodes as a function of their area. The larger capacitance of PEDOT:PSS results in lower turning frequencies.

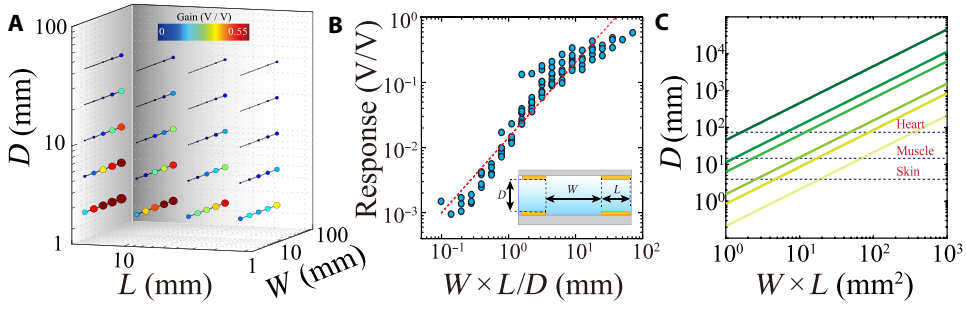

Fig. 4. IC transmission depth scales with TX array geometry and operating voltage to enable low-voltage, long-range, and geometrically scalable communication in physiological environments. (**A**) Effect of electrode geometry (*W*, *D*, and *L*) on IC response above f_{IC} frequencies. Larger and warmer colored symbols correspond to larger responses. Each datapoint is determined by extracting the average response of 256 cycles per frequency. (**B**) IC response is linearly positively correlated with the product of *W* and *L*, and linearly negatively correlated with *D*. Inset: Cross-sectional schematic illustrating geometrical parameters of IC device. The blue medium between TX and RX arrays represents the biological tissue; *D* is the depth of TX inside tissue, *W* is the interelectrode distance of TX or RX pairs, and *L* is the length of square electrodes. (**C**) Estimated communication depth of IC based on electrode geometry and operating voltage (1, 5, 10, 50, 100, and 500 mV; darker shades denote higher voltages). The dashed lines denote the approximate distances between the surface and implants in various human tissues.

(Fig. 5A). Therefore, using a practical consideration for transmission fidelity of 10 × τ, it would be practically possible to reach 14-MHz communication [1/(10 × τ)] with a single IC line. With currently available commercial, discrete amplifiers, we were able to effectively receive and decode digital pulses transmitted up to 6 MHz (fig. S11).

Many bioelectronic devices require multiple parallel lines of data communication, so we explored whether this functionality could be attained using IC. With parallel lines, the rate of data communication can be markedly increased without necessitating higher operating frequency. This approach would only be feasible if individual IC links (RX and TX pairs) could maintain independent transmission in the absence of cross-talk. We therefore designed an experiment where the physical location of the RX pair could be offset with respect to the TX pair (Fig. 5B, inset). The most effective communication (highest response across frequency range) was observed when the RX and TX electrodes were directly aligned. Upon reaching misalignments larger than the electrode geometry (*L*), a notable decay in response was observed (Fig. 5, B and C). Because the response dropped sharply at the boundary of the TX/RX electrode overlap, it is theoretically possible to create a densely packed conformable array of IC transmitters in coaxial format without introducing cross-talk between the independent transmitters. To test this notion, we next fabricated a conformable array of 10 miniaturized IC TX-RX arrays on a parylene C substrate and bonded them directly to rigid or flexible printed circuits (Fig. 5D and fig. S12). Each IC channel was able to operate independently at approximately 6 MHz with minimal cross-talk in this setting (Fig. 5E, red). We then combined operation of all 10 channels to achieve an overall digital communication speed of up to 60 Mbps (Fig. 5E, green). To evaluate signal transmission quality in a physiologic environment, we concurrently operated IC while recording the noise level across the physiologic frequency spectrum using a conventional neural acquisition system sampling from the same medium (Fig. 5F and Materials and Methods). We used a Manchester coding protocol, in which data bits are represented by either a low then high, or a high then low, state for equal time. This approach creates charge-balanced transmission signals and minimizes direct current components of these signals. The presence of IC components within the medium did not introduce noise into the electrophysiological recordings, suggesting potential for integration into implanted devices designed to assay a variety of biological signals.

Low power consumption is a critical feature for implanted bioelectronic devices. We determined that IC power consumption remains constant across frequency for a given impedance, with higher TX/RX impedance resulting in lower consumption across all data rates (Fig. 6A). Given these properties, IC would be capable of transmitting data from a range of clinical and research implanted devices with low power consumption. We compared IC communication efficiency (defined by power consumption relative to operation speed) to other data transmission approaches. Because IC efficiently operates at low voltages, its communication efficiency surpassed the majority of wireless communication protocols used for such devices (Fig. 6B and table S1). IC operates by application of megahertz-range signals to tissue; thus, we also took the guidelines for power injection based on the International Commission on Non-Ionizing Radiation Protection into consideration (*42*). We found that the maximum operating voltages as a function of (i) TX array area and (ii) distance between TX electrodes within a pair were well within safety boundaries for induced electric fields in tissue (fig. S13).

To test the ability of IC to practically transmit high–sampling rate, multichannel data such as would be required for advanced bioelectronic devices, we first devised a surgical protocol to enable chronic implantation in a rodent model (Fig. 6C). In addition, IC must be compatible with existing Si-based data acquisition and processing devices. We use mixed conducting particulate composite (*43*) to bond a conformable electrode array to a printed circuit board (PCB) with a neurophysiological acquisition chip (Intan) and a microprocessor to organize acquired data into packets delivered to the attached conformable TX electrodes, each equipped with a nearby encapsulated magnet. A miniaturized battery was used to supply power (Fig. 6C and figs. S14 and S15). The conformable shank was implanted into the brain through a scalp incision and craniotomy. Using a trocar-based surgical approach (*44*), the TX array and battery were tunneled into the subcutaneous space over the dorsal aspect of the rat's neck. All surgical incisions were then closed, resulting in a fully implanted device capable of transcutaneous data transmission. Two miniaturized external magnets were used both as RX electrodes and for fiducial alignment with the implanted TX electrodes. Signals

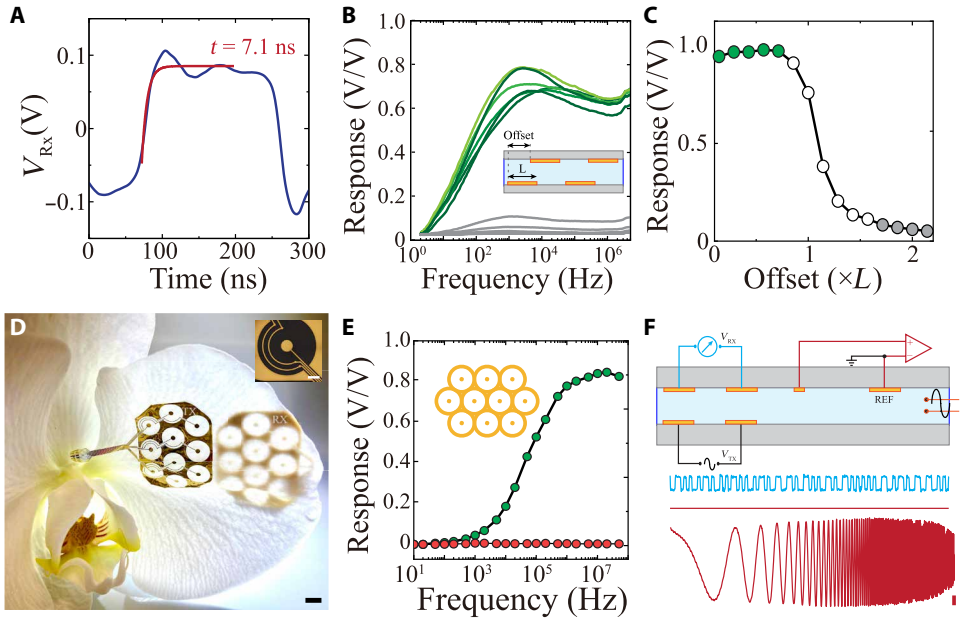

Fig. 5. IC establishes high-bandwidth, digital, parallel data communication using conformable electronic substrates. (**A**) Received square pulse at the RX before slicing and digitization. The red trace is the exponential fit of the IC RX voltage before digitization, resulting in a time constant of 7.1 ns (W, L, D = 5 mm). (**B**) Comparison of frequency responses acquired when RX and TX arrays were positioned inside (green) and outside (gray) line of sight. Inset: Cross-sectional schematic illustrating the experimental setup for measuring IC response at various offsets between TX and RX pairs. (**C**) The response of IC as a function of RX and TX positional offset. Green markers show IC response for positions where the RX is within TX's line of sight, whereas unfilled and gray markers indicate partial alignment or full misalignments of TX and RX, respectively (L = 25 mm). (**D**) Four-micrometer-thick, parallelized (10 links) IC TX and RX arrays conforming to the surface of an orchid petal; scale bar, 5 mm. Optical micrograph of one of the coaxial-shaped IC links; scale bar, 500 μm. (**E**) Frequency response of 10-link IC-based communication resulting in stable high response at ~60 MHz bandwidth (black). The red trace shows the absence of cross-talk between two nearby RX and TX pairs. (**F**) Cross-sectional schematic of simultaneous electrophysiological recording and digital IC signal transmission (with 2-MHz, 50-mV amplitude V_{TX}). Lower blue traces show the extracted digital at RX before digitization, and the two red traces are concurrent electrophysiological measurements of ground (top) or a sweep signal (bottom; 1 to 10 KHz; scale bar, 1 mV amplitude). The RMS noise of electrophysiologic (0.1 to 7500 Hz) recordings during operation of IC was 2.7 μV_{rms} compared to 2.4 μV_{rms} without IC operation.

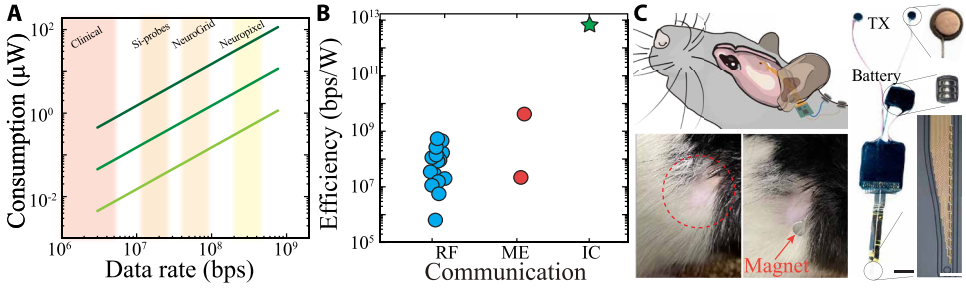

Fig. 6. IC enables fully implantable, noninvasive, ultralow power, stable, and high-speed communication for implantable devices. (**A**) Power consumption of IC as a function of data rate and TX electrode impedance (1, 10, and 100 kilohms dark to light). The shaded areas highlight the required data communication bandwidth for using the denoted neural interface devices. (**B**) Efficiency of implantable communication systems derived as the ratio of bandwidth to power consumption for RF waves, mechanical waves (ME), and IC. (**C**) Simplified schematic of the placement and location of the implant in a rat (top left). Complete embedded system with conformable probe and battery before implantation (right; black scale bar, 5 mm; white scale bar, 50 μm). Location of incision for positioning IC electrode 1 week after surgery (bottom left). RX is aligned transcutaneously via the fiducial magnet of the implanted TX array.

were decoded by a differential amplifier attached to the RX electrodes (fig. S9).

With this setup, we designed a series of experiments to evaluate the ability of IC to transmit chronic intracranial encephalography signals from multichannel implantable probes in freely moving rats. Rats implanted with IC devices had normal behavior without indications of discomfort, and neural signals were transmitted via IC while the animals successfully performed behavioral tasks on an open field maze (movie S1). IC established high-speed communication for simultaneous real-time transmission of 32-channel data across intact cutaneous tissue with minimum distortion in vivo (fig. S16, A and B). The RX array was attached and detached repetitively without adversely affecting signal quality. Transmitted LFP exhibited identifiable state-dependent time-frequency characteristics (Fig. 7, A and B, and fig. S16C) and typical waveform features corresponding to hippocampal area CA1 layers (Fig. 7c). We also compared quality of

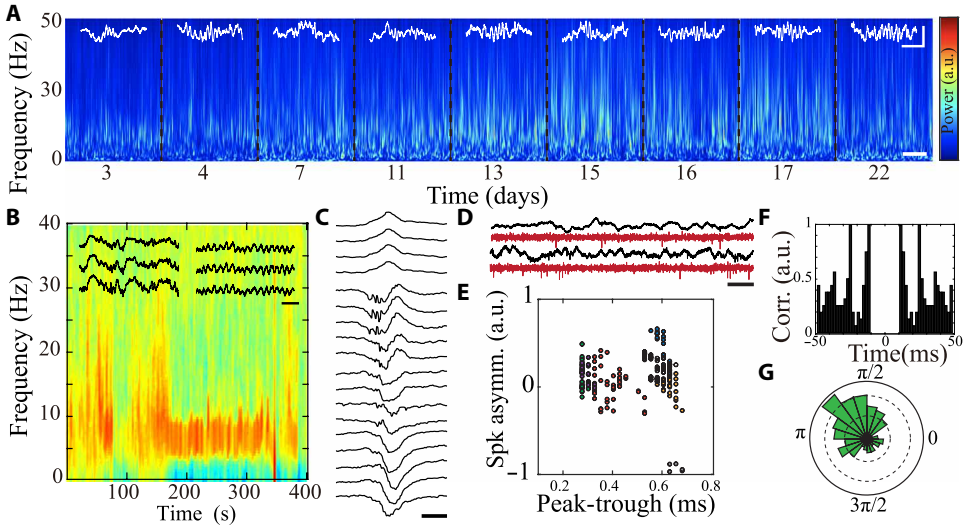

Fig. 7. IC enables stable, chronic communication for implantable devices at the resolution of single neurons in vivo. (**A**) Long-term, time-frequency spectrogram of LFP transmitted by IC from a freely moving rat. Each block notated by dashed lines represents data extracted from a separate recording session (scale bar, 15 s). Superimposed white traces illustrate waveform traces of sleep spindles (scale bar, 250 μV, 100 ms). (**B**) Spectrogram of NREM transitioning to REM sleep with superimposed traces of delta waves and sleep spindles during NREM, as well as theta oscillation during REM sleep (scale bar, 200 ms). (**C**) Sample ripple with clear spatial profile across hippocampal CA1 layers (scale bar, 50 ms). (**D**) Sample LFP traces (top) and their corresponding filtered traces (>500 Hz; bottom) with visible neural spiking activity; scale bar, 50 ms. (**E**) Scatterplot of waveform characteristics of putative single units transmitted by the IC in a freely moving rat. Each symbol corresponds to an average spike waveform of 20 spikes from a putative isolated neuron; colors represent different clustered neurons. (**F**) Sample autocorrelation of a putative clustered neuron transmitted by the IC in a freely moving rat. (**G**) Phase-locking of sample putative single unit's spikes to cortical gamma oscillation ($P < 0.01$, circular mean statistics mu = 0.005, $\kappa = 2.33 \times 10^4$).

signals transmitted via IC and conventional serial peripheral interface (SPI) cables. We found that neural activity patterns did not differ with regard to frequency or duration between the methods (figs. S17 and S18A). Power spectral density of the wideband-transmitted signals was also indistinguishable (fig. S18B), demonstrating that IC does not introduce additional noise or spurious signals into neural data.

Furthermore, IC supported data sampled at 20 KHz, permitting acquisition of neural spiking data. Identifying action potentials originating from individual neurons (spike sorting) is precisely dependent on the shape of each action potential waveform (1- to 2-ms duration), and hence, any signal contamination would prevent identification of spiking clusters. We used a conventional spike-sorting algorithm and were able to identify multiple putative individual neurons with stable waveforms and typical physiologic firing patterns (Fig. 7, D and E). These data support the ability of IC to reliably transmit some of the most exacting biological signals.

To evaluate the stability of IC in vivo, we performed multiple recording sessions in freely moving rodents over a period of 3 weeks after device implantation. Physiologic spectral features of the transmitted signals were maintained across these sessions (Fig. 7A), and detected neural activity patterns exhibited consistent amplitude, duration, and frequency over weeks (fig. S19). Together, these results indicate that IC is fully capable of high-quality and long-term signal transmission in naturalistic in vivo environments, suggesting broad applicability to a range of implanted devices.

DISCUSSION

We developed a biologically based data communication method, IC, that leverages the high ionic conductivity of body fluids to transmit electrical signals across an intact tissue interface. We demonstrated that physiologic ion concentrations in polarizable media support storage of electrical potential energy that can be remotely sensed in a frequency-dependent manner. The IC components (TX/RX arrays) are amenable to miniaturization and can transmit across a tissue distance several times the distance between electrodes within an array at physiologically acceptable voltage operation (4× at 30 mV, 11× at 100 mV). With appropriate geometric design, IC can be used to establish multiple cross-talk–free parallel data lines. IC requires low voltages for operation and has power consumption substantially less than conventional communication methods, such as RF or ultrasound. In addition, IC transmits high sampling rate data with high fidelity and is resistant to disruption by movements of the organism. IC can be integrated with a variety of implantable devices and permits communication through an intact tissue interface, eliminating the need for extruding electronic components. We show that IC is capable of consistent transmission of neural signals, including LFP and individual action potentials, from freely moving rats over a period of at least 3 weeks, confirming feasibility for a variety of in vivo applications.

Materials required for IC are biocompatible and commercially available, and IC arrays are fabricated using established microfabrication techniques (*45*). Because IC uses the intrinsic conductivity of tissue, its operation is not impaired by exposure to water or ions, and we use a charge-balanced coding protocol to minimize the possibility of ion trapping at the array electrodes. The RX/TX arrays do not require encapsulation in biological environments, unlike the modulators used for RF-based methods. Furthermore, IC components are flexible because of their small cross-sectional diameter and ability to be embedded within conformable plastic substrates. Their simple design could also be executed with soft and biodegradable materials, eliminating the need for device removal in circumstances

when time-limited monitoring or intervention is necessary. Although we demonstrate compatibility with Si-based electronic components for signal acquisition here, IC could be easily integrated with a variety of soft, organic electronics to establish fully conformable implantable electronic devices with no rigid components (*14*, *46*, *47*). Although power-carrying components require encapsulation to prevent leakage currents from entering tissues, the low operating voltage of IC potentially permits use of thin, conformable materials for this purpose. IC can currently be powered using implantable batteries, but alternative methods that provide rechargeable power could be considered given its low consumption (*48*). IC transmission lines do not have inherent directionality, raising the possibility of bidirectional communication through parallel lines for active devices such as stimulators.

We demonstrated how IC benefits acquisition of high spatiotemporal resolution neurophysiologic data, but it could be applied to a variety of signals. In large-animal models or human subjects, where implant sizes in the range of centimeters are possible, IC can be configured to transmit across tissue depths of 10 cm, creating opportunities for signal transmission from visceral organs. On the other hand, transmitting across subcutaneous tissue (a few millimeters in thickness) enables miniaturization of RX/TX arrays and utility in small-animal models. Implantation of neural recording arrays integrated with IC enabled complete closure of all incisions, abolishing potential for infection, inflammation, and hemorrhage that can accompany persistent breaches of the tissue interface. IC-based recording was stable over weeks in freely moving animals, and consistently high data quality permitted identification and monitoring of action potentials from individual neurons, a process that requires high sampling rate (10 to 20 KHz) and signal-to-noise ratio (*22*). Although we sampled data intermittently in real time, advances in local storage technology could realize an alternative protocol whereby signals are initially stored within the organism, then transmitted at a later time (*49*). For instance, the high-speed and parallelized lines of IC presented here allow mass transmission, with approximately 2-min time required for 1 GB of data, equivalent of 1 hour of 256-channel clinical data sampled at 512 Hz. The requirement for physical contact between the TX and RX of the IC also ensures that sensitive clinical data are not errantly received or intercepted. Overall, IC offers unique features that could simplify and enhance data transmission from implanted bioelectronic devices, with clinical applicability to procedures ranging from glucose-sensing to brain-machine interfaces.

MATERIALS AND METHODS

Material

PEDOT:PSS (Clevios PH1000) was purchased from Heraeus. D-Sorbitol (≥99.5%; BioUltra), (3-glycidyloxypropyl)trimethoxysilane (GOPS), 4-dodecyl benzene sulfonic acid (DBSA), PBS tablets, and 3-(trimethoxysilyl)propyl methacrylate (A-174 silane) were purchased from Sigma-Aldrich. Micro 90 concentrated cleaning solution was purchased from Special Coating Services. AZnLOF2020 (negative photoresist), AZ9260 (positive photoresist), AZ 400 K, and AZ 300 metal ion–free developers were acquired from MicroChemicals, Merck. Neodymium magnets were purchased from K&J Magnetics (DH101, D301). PCB circuits were manufactured by Eurocircuits. Electronic components were ordered from Digi-key. Type 321 0.002″ stainless steel sheet was purchased from SSTW. Gold plating solution was purchased from Gold Plating Services.

Electrical and frequency characterization

Frequency responses for IC devices were recorded with a battery-powered oscilloscope (Micsig TO1104), a Keysight DSOX2002A oscilloscope, and Keysight 33509B waveform generator. Sine waves were delivered to the TX electrodes using the waveform generator with electrodes terminated by a 50-ohm resistor and monitored by the Keysight oscilloscope. Both oscilloscopes were synchronized with the signal generator by an opto-decoupler (D213, SparkFun). Voltage on the RX electrodes was monitored with the battery-powered oscilloscope, which has a floating ground relative to the TX systems. For each measured frequency, sine waves applied to the TX and received from the RX were averaged 256 times, and the response was calculated using the ratio of RX signal amplitude/TX signal amplitude.

Electrochemical impedance

EIS, modeling, and equivalent circuit extraction were performed with Gamry Reference 600+ using a three-electrode configuration with Ag/AgCl electrodes as counter and reference electrodes. Electrochemical impedance was measured in potentiostatic mode with 100 mV RMS and frequency range from 1 Hz to 5 MHz (10 points per decade).

Conformable device fabrication

A 1.5-μm-thick parylene C layer was coated on double side–polished quartz wafers (100-mm outer diameter, thickness of 550 μm) using an SCS Labcoater 2. Metal electrodes and interconnects were patterned by a metal lift-off process. A 10-nm-thick Ti adhesion layer, followed by a 150-nm-thick Au layer, was deposited (Angstrom EvoVac Multi-Process). A second layer of parylene C (insulation layer), followed by an additional sacrificial layer of parylene C (for the subsequent peel-off process), was deposited similarly to the first layer. During chemical vapor deposition of the second Pa-C layer, 3-(trimethoxysilyl)propyl methacrylate (A-174 silane) was used to enhance adhesion between the first and second layers. Spin-coated antiadhesion agent (5 weight % Micro-90 diluted in DI) reduced the adhesion between the second and third layers. The stacked layers were patterned with a 4.6-μm-thick AZ9260 photoresist and dry etched with an O_2 plasma reactive ion etching process (Oxford Plasmalab 80) to shape the IC electrodes and electrical contact pads. The PEDOT:PSS formulation was prepared on the basis of previously described methods (*43*, *47*). Spin-coated PEDOT:PSS films were patterned by peeling off the third parylene layer.

Animal surgical procedure

All animal experiments were approved by the Institutional Animal Care and Use Committee of Columbia University. Implantations were performed in the somatosensory cortex and/or hippocampus of 10 male Long Evans rats (250 to 350 g; 8 to 11 weeks of age). The animals were housed in a regular 12-hour/12-hour light/dark cycle. No prior experimentation had been performed on these rats. Before the surgical procedure, the rats were housed in pairs, and they were separated after implantation. The animals were initially anesthetized with 2% isoflurane and maintained under anesthesia with 0.75 to 1% isoflurane during the surgery. Craniotomy was performed at coordinates anterior-posterior −3.5 mm, medial-lateral 3 mm, with dorsal-ventral −1.0 mm for somatosensory cortex and −2.0 mm for hippocampus. Dura mater was removed individually, and the probes were inserted into the target areas. The craniotomies were covered with gel foam and sealed using a silicone elastomer. Inspired by

procedures used in epilepsy surgery, we developed a trocar-based tunneling approach using an 18-gauge stainless steel needle to guide the IC transmitter electrodes through the subcutaneous tissue and allow placement without any additional incisions. A suture was used as a guideline that was anchored to the device and the battery. Subsequently, the suture was removed. The mechanical conformability and surface energy of the array substrate facilitate its physical stability within this space. Two #000-gauge stainless steel screws were fixed on the skull above the cerebellum and used as ground and reference electrodes. After implantation, the rats were able to move freely. For data transmission via IC, the RX array was placed on the intact skin surface, which was coated in a thin layer of Tensive conductive adhesive gel (obtained from Parker), and aligned with the TX array via fiducial magnets. A subset of rats were simultaneously implanted with hardware for data transmission via SPI cable to enable direct comparison with IC.

RF propagation depth characterization

A 5 × 6–mm 2.4-GHz BLE module (HJ-580xp, Hongjia), with DA14580 BLE controller and 1005 ceramic 2.4-GHz antenna (TX_{pwr} = +0 dBm, antenna gain = 0.5 dBi), is coated with a thin layer of medical-grade silicone and then immersed into a large bath of PCB. Mechanical manipulators were used to control the depth of the device in the bath. Another similar BLE module is placed on top of the solution to allow characterization of the connection and received signal strength indicator (RSSI). BLE modules are placed facing each other to achieve the best antenna performance. The RSSI of each depth is measured five times, and the distance continued until the depth that was not able to establish a connection.

Real-time digital implantable IC-based device

One onboard microcontroller (μC, STM32F413CHU6, STMicroelectronics) coordinated neural data acquisition (RHD2132, INTAN Technologies) and processing of digital data for IC communication. The device was in the low-power sleep mode after implantation. Once the magnetic trigger signal was detected by alignment of RX with implanted TX, the device began acquiring electrophysiological data and transmitting digitized data. The μC configured the parameters for the neural acquisition chip and established an SPI communication. Sixteen-bit digitized neural data were then acquired periodically through the SPI interface. Data were handled by direct memory access (DMA) unit and then buffered into random-access memory (RAM). IC transmission routine was encoded into charged balanced code using a look-up table and transmitted using a universal asynchronous receiver-transmitter (UART) module. Digital logic signals were attenuated 100 times, high-pass filtered (f_C = 100 KHz), and sent to the TX electrodes.

Implantable magnetic IC electrodes

Stainless steel foil (50 μm thick) was soldered to a medical-grade silicone-jacket–based wire to serve as the IC electrode. A 5-mm magnet was then attached to the back of the electrode, and the whole assembly was potted by a thin layer of medical-grade silicone, excluding the electrode surface.

IC receiver with automatic gain control

A low-noise operational amplifier (OPA2320, Texas Instruments) served as a buffer for the signal received from IC electrodes. Then, the signal is bandpassed (100 kHz to 3 MHz) and amplified with a variable gain amplifier with automatic gain control (AD8338, Analog Device). The differential output signal is then converted to logic level by a high-speed low-voltage differential signaling receiver (FIN1002, ON Semiconductor). Last, a μC (STM32F723ZET, STMicroelectronics) receives the logic levels through a UART module and transmits the data to a computer through a USB.

Validation of electrophysiological recording

In vivo recordings were manually classified into wake, rapid eye movement (REM), and non-REM (NREM) epochs based on theta/delta ratio with additional movement information extracted from the onboard accelerometer. An amplitude-threshold method was used to detect spikes from bandpass–filtered data (0.25 to 2.5 kHz), and spike waveforms were retrieved from wide-band files. Cell clustering was done by an unsupervised expectation-maximization algorithm (Klustakwik). Rats also performed free exploration of an open field maze, allowing demonstration of walking, running, and rearing behaviors during recording.

LFP and spike analysis

We used custom MATLAB software to score behavior into NREM sleep, REM sleep, and waking epochs based on spectral features and an onboard accelerometer. Spectral analyses were generated using Gabor-based analytical wavelet. Spike waveform characterization was performed by first calculating an average waveform for each 20 spikes and then determining peak time and peak asymmetry for each averaged waveform.

SUPPLEMENTARY MATERIALS

Supplementary material for this article is available at https://science.org/doi/10.1126/sciadv.abm7851

REFERENCES AND NOTES

1. E. Krook-Magnuson, J. N. Gelinas, I. Soltesz, G. Buzsáki, Neuroelectronics and biooptics: Closed-loop technologies in neurological disorders. *JAMA Neurol.* **72**, 823–829 (2015).
2. P. Jastrzebska-Perfect, S. Chowdhury, G. D. Spyropoulos, Z. Zhao, C. Cea, J. N. Gelinas, D. Khodagholy, Translational neuroelectronics. *Adv. Funct. Mater.* **30**, 1909165 (2020).
3. T. Someya, Z. Bao, G. G. Malliaras, The rise of plastic bioelectronics. *Nature* **540**, 379–385 (2016).
4. T. A. Szuts, V. Fadeyev, S. Kachiguine, A. Sher, M. V. Grivich, M. Agrochão, P. Hottowy, W. Dabrowski, E. V. Lubenov, A. G. Siapas, N. Uchida, A. M. Litke, M. Meister, A wireless multi-channel neural amplifier for freely moving animals. *Nat. Neurosci.* **14**, 263–269 (2011).
5. S. M. Won, L. Cai, P. Gutruf, J. A. Rogers, Wireless and battery-free technologies for neuroengineering. *Nat. Biomed. Eng.* 10.1038/s41551-021-00683-3 (2021).
6. C. Y. Kim, M. J. Ku, R. Qazi, H. J. Nam, J. W. Park, K. S. Nam, S. Oh, I. Kang, J. H. Jang, W. Y. Kim, J. H. Kim, J. W. Jeong, Soft subdermal implant capable of wireless battery charging and programmable controls for applications in optogenetics. *Nat. Commun.* **12**, 535 (2021).
7. D. Seo, R. M. Neely, K. Shen, U. Singhal, E. Alon, J. M. Rabaey, J. M. Carmena, M. M. Maharbiz, Wireless recording in the peripheral nervous system with ultrasonic neural dust. *Neuron* **91**, 529–539 (2016).
8. D. K. Piech, B. C. Johnson, K. Shen, M. M. Ghanbari, K. Y. Li, R. M. Neely, J. E. Kay, J. M. Carmena, M. M. Maharbiz, R. Muller, A wireless millimetre-scale implantable neural stimulator with ultrasonically powered bidirectional communication. *Nat. Biomed. Eng.* **4**, 207–222 (2020).
9. D. A. Borton, M. Yin, J. Aceros, A. Nurmikko, An implantable wireless neural interface for recording cortical circuit dynamics in moving primates. *J. Neural Eng.* **10**, 026010 (2013).
10. P. Jin, J. Fu, F. Wang, Y. Zhang, P. Wang, X. Liu, Y. Jiao, H. Li, Y. Chen, Y. Ma, X. Feng, A flexible, stretchable system for simultaneous acoustic energy transfer and communication. *Sci. Adv.* **7**, abg2507 (2021).
11. L. J. Challis, Mechanisms for interaction between RF fields and biological tissue. *Bioelectromagnetics* **26**, S98–S106 (2005).

12. E. R. Adair, R. C. Petersen, Biological effects of radiofrequency/microwave radiation. *IEEE Trans. Microw. Theory Tech.* **50**, 953–962 (2002).
13. IEEE Standard for Safety Levels with Respect to Human Exposure to Radio Frequency Electromagnetic Fields, 3 kHz to 300 GHz. **16**, 1–83 (1999).
14. A. Zhou, S. R. Santacruz, B. C. Johnson, G. Alexandrov, A. Moin, F. L. Burghardt, J. M. Rabaey, J. M. Carmena, R. Muller, A wireless and artefact-free 128-channel neuromodulation device for closed-loop stimulation and recording in non-human primates. *Nat. Biomed. Eng.* **3**, 15–26 (2019).
15. M. Yin, D. A. Borton, J. Komar, N. Agha, Y. Lu, H. Li, J. Laurens, Y. Lang, Q. Li, C. Bull, L. Larson, D. Rosler, E. Bezard, G. Courtine, A. V. Nurmikko, Wireless neurosensor for full-spectrum electrophysiology recordings during free behavior. *Neuron* **84**, 1170–1182 (2014).
16. A. Khalifa, Y. Karimi, Q. Wang, S. Garikapati, W. Montlouis, M. Stanacevic, N. Thakor, R. Etienne-Cummings, The microbead: A highly miniaturized wirelessly powered implantable neural stimulating system. *IEEE Trans. Biomed. Circuits Syst.* **12**, 521–531 (2018).
17. I. V. Meglinski, S. J. Matcher, Quantitative assessment of skin layers absorption and skin reflectance spectra simulation in the visible and near-infrared spectral regions. *Physiol. Meas.* **23**, 741–753 (2002).
18. T. G. Zimmerman, Personal area networks: Near-field intrabody communication. *IBM Syst. J.* **35**, 609–617 (1996).
19. S. Il Chang, K. Alashmouny, M. McCormick, Y. C. Chen, E. Yoon, BioBolt: A minimally-invasive neural interface for wireless epidural recording by intra-skin communication. *IEEE Symp. VLSI Circuits, Dig. Tech. Pap.* 146–147 (2011).
20. E. Stavrinidou, P. Leleux, H. Rajaona, D. Khodagholy, J. Rivnay, M. Lindau, S. Sanaur, G. G. Malliaras, Direct measurement of ion mobility in a conducting polymer. *Adv. Mater.* **25**, 4488–4493 (2013).
21. G. Buzsáki, E. Stark, A. Berényi, D. Khodagholy, D. R. Kipke, E. Yoon, K. D. Wise, Tools for probing local circuits: High-density silicon probes combined with optogenetics. *Neuron* **86**, 92–105 (2015).
22. K. D. Harris, D. A. Henze, J. Csicsvari, H. Hirase, G. Buzsáki, Accuracy of tetrode spike separation as determined by simultaneous intracellular and extracellular measurements. *J. Neurophysiol.* **84**, 401–414 (2000).
23. J. J. Jun, N. A. Steinmetz, J. H. Siegle, D. J. Denman, M. Bauza, B. Barbarits, A. K. Lee, C. A. Anastassiou, A. Andrei, Ç. Aydın, M. Barbic, T. J. Blanche, V. Bonin, J. Couto, B. Dutta, S. L. Gratiy, D. A. Gutnisky, M. Häusser, B. Karsh, P. Ledochowitsch, C. M. Lopez, C. Mitelut, S. Musa, M. Okun, M. Pachitariu, J. Putzeys, P. D. Rich, C. Rossant, W. Sun, K. Svoboda, M. Carandini, K. D. Harris, C. Koch, J. O'Keefe, T. D. Harris, Fully integrated silicon probes for high-density recording of neural activity. *Nature* **551**, 232–236 (2017).
24. D. Khodagholy, J. N. Gelinas, T. Thesen, W. Doyle, O. Devinsky, G. G. Malliaras, G. Buzsáki, NeuroGrid: Recording action potentials from the surface of the brain. *Nat. Neurosci.* **18**, 310–315 (2015).
25. B. Lee, M. N. Zubair, Y. D. Marquez, D. M. Lee, L. A. Kalayjian, C. N. Heck, C. Y. Liu, A single-center experience with the NeuroPace RNS system: A review Of techniques and potential problems. *World Neurosurg.* **84**, 719–726 (2015).
26. B. C. Jobst, R. Kapur, G. L. Barkley, C. W. Bazil, M. J. Berg, G. K. Bergey, J. G. Boggs, S. S. Cash, A. J. Cole, M. S. Duchowny, R. B. Duckrow, J. C. Edwards, S. Eisenschenk, A. J. Fessler, N. B. Fountain, E. B. Geller, A. M. Goldman, R. R. Goodman, R. E. Gross, R. P. Gwinn, C. Heck, A. A. Herekar, L. J. Hirsch, D. King-Stephens, D. R. Labar, W. R. Marsh, K. J. Meador, I. Miller, E. M. Mizrahi, A. M. Murro, D. R. Nair, K. H. Noe, P. W. Olejniczak, Y. D. Park, P. Rutecki, V. Salanova, R. D. Sheth, C. Skidmore, M. C. Smith, D. C. Spencer, S. Srinivasan, W. Tatum, P. Van Ness, D. G. Vossler, R. E. Wharen, G. A. Worrell, D. Yoshor, R. S. Zimmerman, T. L. Skarpaas, M. J. Morrell, Brain-responsive neurostimulation in patients with medically intractable seizures arising from eloquent and other neocortical areas. *Epilepsia* **58**, 1005–1014 (2017).
27. U. Topalovic, Z. M. Aghajan, D. Villaroman, S. Hiller, L. Christov-Moore, T. J. Wishard, M. Stangl, N. R. Hasulak, C. S. Inman, T. A. Fields, V. R. Rao, D. Eliashiv, I. Fried, N. Suthana, Wireless programmable recording and stimulation of deep brain activity in freely moving humans. *Neuron* **108**, 322–334.e9 (2020).
28. L. R. Hochberg, M. D. Serruya, G. M. Friehs, J. A. Mukand, M. Saleh, A. H. Caplan, A. Branner, D. Chen, R. D. Penn, J. P. Donoghue, Neuronal ensemble control of prosthetic devices by a human with tetraplegia. *Nature* **442**, 164–171 (2006).
29. M. Velliste, S. Perel, M. C. Spalding, A. S. Whitford, A. B. Schwartz, Cortical control of a prosthetic arm for self-feeding. *Nature* **453**, 1098–1101 (2008).
30. G. Buzsáki, Large-scale recording of neuronal ensembles. *Nat. Neurosci.* **7**, 446–451 (2004).
31. M. J. Morrell; RNS System in Epilepsy Study Group, Responsive cortical stimulation for the treatment of medically intractable partial epilepsy. *Neurology* **77**, 1295–1304 (2011).
32. R. W. P. King, B. S. Trembly, J. W. Strohbehn, The electromagnetic field of an insulated antenna in a conducting or dielectric medium. *IEEE Trans. Microw. Theory Tech.* **31**, 574–583 (1983).
33. D. C. Grahame, The electrical double layer and the theory of electrocapillarity. *Chem. Rev.* **41**, 441–501 (1947).
34. J. Israelachvili, *Intermolecular and Surface Forces* (Elsevier, 2011).
35. J. Li, Y. Dong, J. H. Park, J. Yoo, Body-coupled power transmission and energy harvesting. *Nat. Electron.* **4**, 530–538 (2021).
36. K. Hachisuka, T. Takeda, Y. Terauchi, K. Sasaki, H. Hosaka, K. Itao, Intra-body data transmission for the personal area network. *Microsyst. Technol.* **11**, 1020–1027 (2005).
37. J. Rosell, J. Colominas, P. Riu, R. Pallas-Areny, J. G. Webster, Skin impedance from 1 Hz to 1 MHz. *I.E.E.E. Trans. Biomed. Eng.* **35**, 649–651 (1988).
38. C. Gabriel, *Compilation of the Dielectric Properties of Body Tissues at RF and Microwave Frequencies* (King's Coll London (United Kingdom) Dept of Physics, 1996).
39. X. Cui, D. C. Martin, Electrochemical deposition and characterization of poly(3,4-ethylenedioxythiophene) on neural microelectrode arrays. *Sens. Actuators B* **89**, 92–102 (2003).
40. K. Tybrandt, I. V. Zozoulenko, M. Berggren, Chemical potential–electric double layer coupling in conjugated polymer–polyelectrolyte blends. *Sci. Adv.* **3**, eaao3659 (2017).
41. D. Khodagholy, T. Doublet, P. Quilichini, M. Gurfinkel, P. Leleux, A. Ghestem, E. Ismailova, T. Hervé, S. Sanaur, C. Bernard, G. G. Malliaras, In vivo recordings of brain activity using organic transistors. *Nat. Commun.* **4**, 1575 (2013).
42. International Commission on Non-Ionizing Radiation Protection (ICNIRP), Guidelines for limiting exposure to electromagnetic fields (100 kHz to 300 GHz). *Health Phys.* **118**, 483–524 (2020).
43. P. Jastrzebska-Perfect, G. D. Spyropoulos, C. Cea, Z. Zhao, O. J. Rauhala, A. Viswanathan, S. A. Sheth, J. N. Gelinas, D. Khodagholy, Mixed-conducting particulate composites for soft electronics. *Sci. Adv.* **6**, eaaz6767 (2020).
44. Z. Zhao, C. Cea, J. N. Gelinas, D. Khodagholy, Responsive manipulation of neural circuit pathology by fully implantable, front-end multiplexed embedded neuroelectronics. *Proc. Natl. Acad. Sci.* **118**, e2022659118 (2021).
45. D. Khodagholy, J. Rivnay, M. Sessolo, M. Gurfinkel, P. Leleux, L. H. Jimison, E. Stavrinidou, T. Herve, S. Sanaur, R. M. Owens, G. G. Malliaras, High transconductance organic electrochemical transistors. *Nat. Commun.* **4**, 2133 (2013).
46. S. Il Park, D. S. Brenner, G. Shin, C. D. Morgan, B. A. Copits, H. U. Chung, M. Y. Pullen, K. N. Noh, S. Davidson, S. J. Oh, J. Yoon, K. I. Jang, V. K. Samineni, M. Norman, J. G. Grajales-Reyes, S. K. Vogt, S. S. Sundaram, K. M. Wilson, J. S. Ha, R. Xu, T. Pan, T. Il Kim, Y. Huang, M. C. Montana, J. P. Golden, M. R. Bruchas, R. W. Gereau, J. A. Rogers, Soft, stretchable, fully implantable miniaturized optoelectronic systems for wireless optogenetics. *Nat. Biotechnol.* **33**, 1280–1286 (2015).
47. C. Cea, G. D. Spyropoulos, P. Jastrzebska-Perfect, J. J. Ferrero, J. N. Gelinas, D. Khodagholy, Enhancement-mode ion-based transistor as a comprehensive interface and real-time processing unit for in vivo electrophysiology. *Nat. Mater.* **19**, 679–686 (2020).
48. A. Burton, S. M. Won, A. K. Sohrabi, T. Stuart, A. Amirhossein, J. U. Kim, Y. Park, A. Gabros, J. A. Rogers, F. Vitale, A. G. Richardson, P. Gutruf, Wireless, battery-free, and fully implantable electrical neurostimulation in freely moving rodents. *Microsyst. Nanoeng.* **7**, 62 (2021).
49. E. J. Fuller, S. T. Keene, A. Melianas, Z. Wang, S. Agarwal, Y. Li, Y. Tuchman, C. D. James, M. J. Marinella, J. J. Yang, A. Salleo, A. A. Talin, Parallel programming of an ionic floating-gate memory array for scalable neuromorphic computing. *Science* **364**, 570–574 (2019).
50. D. K. Piech, J. E. Kay, B. E. Boser, M. M. Maharbiz, *2017 39th Annual International Conference of the IEEE Engineering in Medicine and Biology Society (EMBC)* (IEEE, 2017), pp. 221–225.
51. J. Lee, V. Leung, A. H. Lee, J. Huang, P. Asbeck, P. P. Mercier, S. Shellhammer, L. Larson, F. Laiwalla, A. Nurmikko, Neural recording and stimulation using wireless networks of microimplants. *Nat. Electron.* **4**, 604–614 (2021).
52. M. Yin, M. Ghovanloo, A low-noise clockless simultaneous 32-channel wireless neural recording system with adjustable resolution. *Analog Integr. Circuits Signal Process.* **66**, 417–431 (2011).
53. H. Miranda, V. Gilja, C. A. Chestek, K. V. Shenoy, T. H. Meng, HermesD: A high-rate long-range wireless transmission system for simultaneous multichannel neural recording applications. *IEEE Trans. Biomed. Circuits Syst.* **4**, 181–191 (2010).
54. A. M. Sodagar, G. E. Perlin, Y. Yao, K. D. Wise, K. Najafi, *An Implantable Microsystem for Wireless Multi-Channel Cortical Recording* (IEEE, 2007), pp. 69–72.
55. S. Imani, A. J. Bandodkar, A. M. V. Mohan, R. Kumar, S. Yu, J. Wang, P. P. Mercier, A wearable chemical–electrophysiological hybrid biosensing system for real-time health and fitness monitoring. *Nat. Commun.* **7**, 11650 (2016).
56. H. Ando, K. Takizawa, T. Yoshida, K. Matsushita, M. Hirata, T. Suzuki, Wireless multichannel neural recording with a 128-Mbps UWB transmitter for an implantable brain-machine interfaces. *IEEE Trans. Biomed. Circuits Syst.* **10**, 1068–1078 (2016).
57. R. Muller, H.-P. Le, W. Li, P. Ledochowitsch, S. Gambini, T. Bjorninen, A. Koralek, J. M. Carmena, M. M. Maharbiz, E. Alon, A minimally invasive 64-channel wireless μECoG implant. *IEEE J. Solid-State Circuits.* **50**, 344–359 (2014).
58. R. R. Harrison, R. J. Kier, C. A. Chestek, V. Gilja, P. Nuyujukian, S. Ryu, B. Greger, F. Solzbacher, K. V. Shenoy, Wireless neural recording with single low-power integrated circuit. *IEEE Trans. Neural Syst. Rehabil. Eng.* **17**, 322–329 (2009).

59. M. Rizk, I. Obeid, S. H. Callender, P. D. Wolf, A single-chip signal processing and telemetry engine for an implantable 96-channel neural data acquisition system. *J. Neural Eng.* **4**, 309–321 (2007).
60. W. Biederman, D. J. Yeager, N. Narevsky, A. C. Koralek, J. M. Carmena, E. Alon, J. M. Rabaey, A fully-integrated, miniaturized (0.125 mm^2) 10.5 μW wireless neural sensor. *IEEE J. Solid-State Circuits.* **48**, 960–970 (2013).
61. G. Gagnon-Turcotte, A. A. Kisomi, R. Ameli, C.-O. D. Camaro, Y. LeChasseur, J.-L. Néron, P. B. Bareil, P. Fortier, C. Bories, Y. De Koninck, A wireless optogenetic headstage with multichannel electrophysiological recording capability. *Sensors* **15**, 22776–22797 (2015).
62. H. U. Chung, B. H. Kim, J. Y. Lee, J. Lee, Z. Xie, E. M. Ibler, K. Lee, A. Banks, J. Y. Jeong, J. Kim, C. Ogle, D. Grande, Y. Yu, H. Jang, P. Assem, D. Ryu, J. W. Kwak, M. Namkoong, J. B. Park, Y. Lee, D. H. Kim, A. Ryu, J. Jeong, K. You, B. Ji, Z. Liu, Q. Huo, X. Feng, Y. Deng, Y. Xu, K.-I. Jang, J. Kim, Y. Zhang, R. Ghaffari, C. M. Rand, M. Schau, A. Hamvas, D. E. Weese-Mayer, Y. Huang, S. M. Lee, C. H. Lee, N. R. Shanbhag, A. S. Paller, S. Xu, J. A. Rogers, Binodal, wireless epidermal electronic systems with in-sensor analytics for neonatal intensive care. *Science* **363**, eaau0780 (2019).
63. N. Ahmadi, M. L. Cavuto, P. Feng, L. B. Leene, M. Maslik, F. Mazza, O. Savolainen, K. M. Szostak, C.-S. Bouganis, J. Ekanayake, *2019 9th International IEEE/EMBS Conference on Neural Engineering (NER)* (IEEE, 2019), pp. 719–724.

Acknowledgments: This work was supported by Columbia University School of Engineering and Applied Science as well as Columbia University Medical Center, Department of Neurology and Institute for Genomic Medicine. The device fabrication was performed at Columbia Nano-Initiative. We thank G. Malliaras (Cambridge University), Y. Borisenkov, J. Vichiconti, N. Ariel-Sternberg (CNI), and all Khodagholy and Gelinas laboratory members for support. We thank W. Villa and S. Santos for managing the administrative affairs related to this project (CU). **Funding:** This work was supported by the National Institutes of Health grants (1U01NS108923-01, R01NS118091, and R21 EY 32381-01), National Science Foundation CAREER award (1944415), and EAGER (2027135). **Author contributions:** D.K., J.N.G., and Z.Z. conceived the project. Z.Z. designed, developed, fabricated, and characterized the materials and devices. C.C. and G.D.S. fabricated the devices. Z.Z. and J.N.G. analyzed the neural data. All authors contributed to the writing of the paper. **Competing interests:** The authors declare that they have no competing interests. **Data and materials availability:** All data needed to evaluate the conclusions in the paper are present in the paper and/or the Supplementary Materials.

Submitted 11 October 2021
Accepted 14 February 2022
Published 6 April 2022
10.1126/sciadv.abm7851

ScienceAdvances

Ionic communication for implantable bioelectronics

Zifang ZhaoGeorge D. SpyropoulosClaudia CeaJennifer N. GelinasDion Khodagholy

Sci. Adv., 8 (14), eabm7851. • DOI: 10.1126/sciadv.abm7851

Science Advances (ISSN) is published by the American Association for the Advancement of Science. 1200 New York Avenue NW, Washington, DC 20005. The title *Science Advances* is a registered trademark of AAAS.